ChemPubSoc Europe

DOI: 10.1002/cctc.201500784

CHEMCATCHEM Full Papers

Aberration-Corrected Transmission Electron Microscopy and In Situ XAFS Structural Characterization of Pt/γ-Al_2O_3 Nanoparticles**

Wharton Sinkler,[a] Sergio I. Sanchez,[a] Steven A. Bradley,[a] Jianguo Wen,[b] Bhoopesh Mishra,[c] Shelly D. Kelly,[a] and Simon R. Bare*[a]

Aberration-corrected (AC) STEM, AC TEM and in situ X-ray absorption fine structure spectroscopy (XAFS) were used to characterize the Pt clusters present on a 0.35 wt% Pt on γ-alumina support after reduction in hydrogen at 700 °C. STEM high-angle annular dark field imaging shows that cluster formation takes place at temperatures up to approximately 350 °C, and this is followed by gradual growth in cluster size for heat treatments in hydrogen up to 700 °C. The STEM data show that after 700 °C reduction the Pt clusters are present in a narrow size distribution centered at 0.88 nm, and using a method involving a redistribution of the Pt atoms using a high electron dosage in the STEM, it is shown that the clusters are present in two-dimensional morphology. This conclusion is verified using intensity line scans. The in situ extended X-ray absorption fine structure data are in good agreement with these observations. High-resolution AC–TEM, which uses a broad coherent electron beam, and can thus offer advantages relative to STEM for structure determination of fine clusters, supported by image simulations of through-focus series, were used to analyze the structures of Pt particles. The structures determined by using AC–TEM are consistent with STEM and EXAFS data in having a flat two-dimensional morphology. Comparison of AC–STEM and AC TEM data for the same 700 °C reduced sample suggests that parallel-beam TEM mode of imaging may be advantageous because of the less pronounced beam-induced structural rearrangements that occur when imaging with a fine STEM probe.

Introduction

Supported noble-metal particles provide key active sites for many industrial catalytic processes such as catalytic reforming.[1] In spite of their scarcity and cost, the high efficacy of noble metals, most particularly Pt, has led to widespread adoption in large-scale catalytic processes in the refining and chemical industries. Control of the catalytic properties of supported noble-metals is critical for developing improved catalysts which enhance yields of desired products in these processes. A central challenge for catalyst characterization is thus to provide structure determinations of supported noble-metal catalytic particles, as well as to determine how structures change owing to variations in support interactions, treatment conditions, and other factors impacting particle growth and coalescence. Only by directly determining these structures can one begin to specify the structural attributes, which are conducive for a particular chemical reaction on one hand, and secondly how distinct synthesis routes may result in different, more effective, catalytic structures. The focus of the current work is to apply state-of-the-art electron microscopic techniques to obtain structural information, ideally direct structure determination, in a model system consisting of platinum particles on a gamma-alumina catalyst support. These advanced microscopy data are supported by complementary in situ X-ray absorption fine structure (XAFS) data, which provide an ensemble-averaged view of the structures. Recent advances in electron microscopy, specifically the availability of aberration correction, have made atomic-level imaging a relatively routine technique in both transmission electron microscopy (TEM) and scanning transmission electron microscopy (STEM). One of the purposes of this paper is to compare and contrast the information provided by these two electron microscopy techniques for determining structures of catalytic nanoparticles, and to compare the data with that from XAFS spectroscopy.

Supported Pt nanoparticles have been extensively studied previously by a plethora of techniques including electron microscopy,[2–4] X-ray absorption spectroscopy,[5–12] and a range of other techniques.[13] An important parameter for controlling

[a] Dr. W. Sinkler, Dr. S. I. Sanchez, Dr. S. A. Bradley, Dr. S. D. Kelly, Dr. S. R. Bare
UOP LLC, a Honeywell Company
Des Plaines IL 60017 (USA)
E-mail: simon.bare@honeywell.com

[b] Dr. J. Wen
Electron Microscopy Center—Center for Nanoscale Materials
Nanoscience and Technology Division
Argonne National Laboratory
Argonne IL 60439 (USA)

[c] Dr. B. Mishra
Physics Department
Illinois Institute of Technology
Chicago, IL, 60016 (USA)

[**] XAFS = X-ray absorption fine structure

Supporting Information for this article is available on the WWW under http://dx.doi.org/10.1002/cctc.201500784.

AEM 3 Part of a Special Issue on Advanced Microscopy and Spectroscopy for Catalysis. A link to the Table of Contents will appear here once the Special Issue is assembled.

the structural and chemical properties of supported metal nanoparticles is the reduction treatment during which cluster formation occurs. Previous studies,[6] including work by the current authors,[14] have found indications that there is a sharp break in the trends of structure development of fine Pt clusters as the treatment temperature in hydrogen exceeds approximately 350 °C, at which the Pt reduction is largely complete. Above this temperature the clusters become flatter as a result of the stronger interaction of the nanoparticle with the oxidic support.[6,14] The possibility of directly determining structures of individual fine Pt clusters is of direct relevance to understanding the changes in cluster evolution with reduction temperature, which may be relevant for performance.[6]

Results

Aberration-corrected STEM

In Figure 1 a–d, aberration-corrected (AC) STEM images of the 0.35 wt% Pt/chlorided γ-alumina sample are shown after reduction in hydrogen at a temperature of 250 °C, 300 °C, 350 °C, and 700 °C, respectively. The fully oxidized state, which is reported elsewhere,[25] shows predominantly isolated Pt atoms with occasional Pt dimers in AC-STEM images. After reduction at 250 °C (Figure 1 a), the sample still shows abundant single atoms of Pt, but association of Pt atoms into incipient clusters of 4–6 atoms is also commonly observed. For the sample reduced at 300 °C, the degree of association of Pt atoms has further increased and the proportion of isolated atoms has decreased. In addition, the images frequently show 0.5–0.7 nm diameter clusters the structure of which is indistinct because of the tendency of such very fine clusters to undergo structural rearrangement under the focused electron beam of the electron microscope. After reduction at 350 °C, further development of clusters is observed and it appears that the majority of Pt atoms are now contained within clusters of approximately 0.5–0.8 nm diameter. Finally, after 700 °C reduction, (Figure 1 d), very few isolated Pt atoms are found and the clusters have slightly increased in size to have an average cluster size of 0.88 nm diameter and they have a narrow particle size distribution, as shown in Figure 2. A representative image of that used to determine the particle size distribution is shown in Supplemental Figure 1.

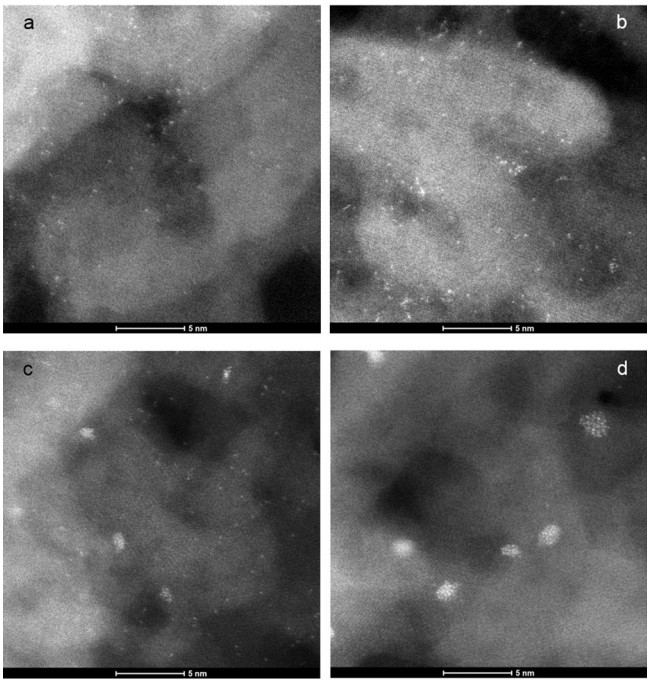

Figure 1. AC–STEM images of Pt clusters on the γ-Al_2O_3 support after hydrogen reduction at a) 250 °C, b) 300 °C, c) 350 °C, and d) 700 °C. Scale bars = 5 nm.

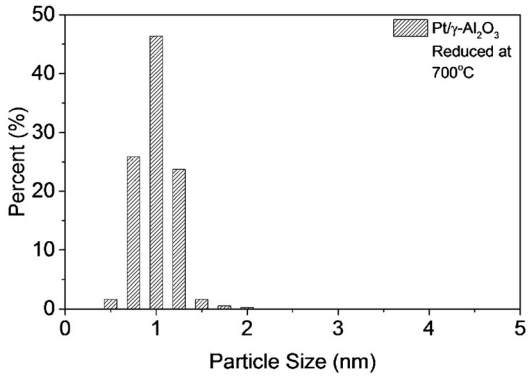

Figure 2. Pt cluster size (diameter) distribution for the 700 °C reduced sample.

Whereas the AC-STEM images show fairly clear images of individual atoms as well as smaller associations of Pt atoms containing less than approximately 6–8 atoms, the images of larger clusters in the range of 0.6–0.8 nm diameter (approximately 8–18 atoms based on the volume per atom for Pt metal) typically can show more of a blur of distinct atoms because of the interaction with the electron beam. A major cause of the difficulty of obtaining structural images for such clusters is the tendency for atoms to displace under the high-energy electron beam, and an additional factor may be the superposition of multiple atomic layers, resulting in projected interatomic distances below the instrument's 0.8 Å resolution. However, as documented below, the use of AC-TEM with its broad coherent electron beam, can offer advantages relative to STEM for detailed atom-resolved structure determination of fine clusters.

To obtain further insight into the three-dimensional structure of the clusters, a method for counting the atoms in individual clusters by dispersing them with the electron beam was employed.[15] In this method, a cluster is imaged in order to measure its diameter, then a higher intensity electron beam is used to fully disperse the clusters, after which the individual atoms can be counted. This method was performed on a range of individual clusters for the same 700 °C hydrogen-reduced sample (Figure 1 d). A deliberate attempt was made to assess the mor-

phology of particles at the extremities of the distribution histogram so that trends in morphology could be elucidated. Therefore, the resulting particle size distribution obtained in Figure 3 will not be representative of the actual size distribution histogram (Figure 2). The results in Figure 3 show the number of Pt

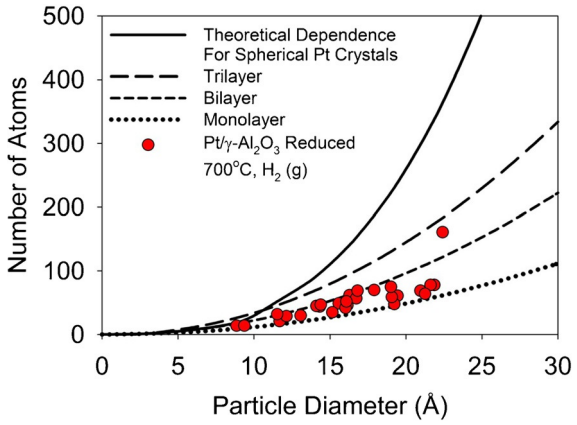

Figure 3. Plot of number of atoms in a cluster vs. particle diameter determined using beam-induced dispersion and atom counting, and AC–STEM imaging. Lines illustrate expected trends for several model cases.

atoms vs. the particle diameter, together with the theoretical values for a number of different cluster shapes such as hemispherical, and 2-dimensional slab-shaped with various thicknesses. As can be seen in the plot, the result of this analysis for the 700 °C sample suggests a morphology that is distinctly 2-dimensional,[26] and shows a pronounced deficit in the numbers of atoms relative to a hemispherical model. For the majority of particles studied by this means, the number of atoms is consistent with a thin slab with thickness intermediate between monolayer and bilayer structures. As confirmation of this novel methodology to determine the thickness of the clusters, a more traditional intensity line scan across several clusters was performed and those data are summarized in the Supporting Information, Figure 2. The intensity of the line scans across a single Pt atom and across a representative cluster is consistent with the cluster having at most a thickness of two atomic layers.

Thus, the AC–STEM data readily allow direct visualization of the Pt atoms in the cluster, allowing (i) a size distribution to be determined (Figure 2), (ii) the morphology of the cluster by atom counting after high electron dose (Figure 3), and (iii) the evolution of the clusters as a function of reduction temperature (Figure 1).

Extended X-ray absorption fine structure (EXAFS)

In Figure 4 the Pt L_3-edge EXAFS data for the 700 °C hydrogen re-reduced sample are shown. The spectrum was recorded in situ at room temperature in a flow of hydrogen after re-reduction of the ex situ reduced sample.

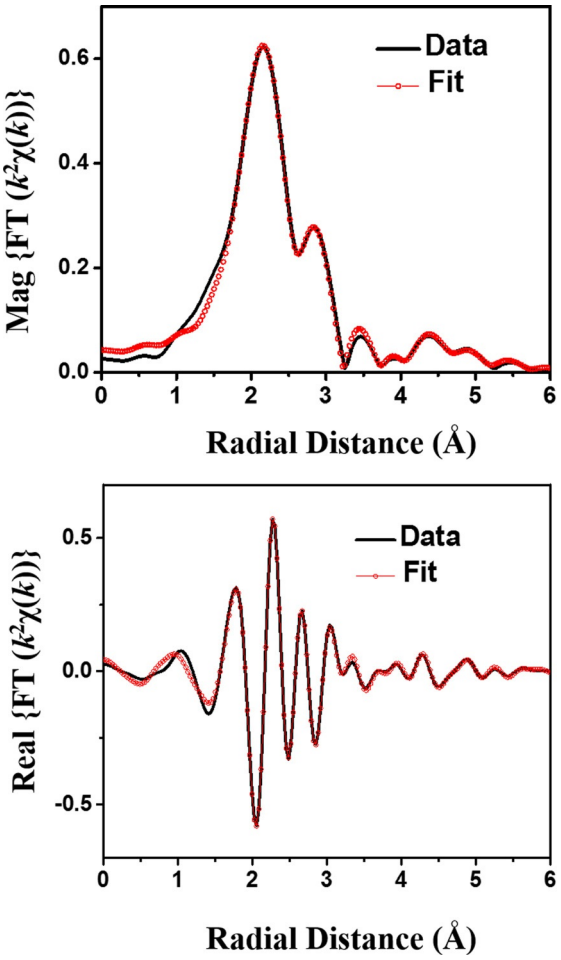

Figure 4. Magnitude (top) and real part (bottom) of the Fourier transform of the Pt L_3-edge EXAFS of the 700 °C reduced catalyst. The data (line) and fit (dotted) are shown.

The EXAFS data were modeled according to the method described in the Experimental Section, and the results are summarized in Table 1 for the single scattering paths.

The first-shell Pt–Pt coordination number of 3.3 implies that the average size of the Pt clusters is small, as this value is substantially lower than the bulk value of 12. Moreover, the lack of a measurable coordination number for the second Pt–Pt scattering path (Pt–Pt2 at 2.7 Å, see below) implies that the clusters are essentially two-dimensional or disk-shaped, in agreement with the STEM data (Figure 3). The average Pt cluster size and shape can be determined from these EXAFS coordination numbers (CN). It has been shown that if coordination numbers beyond the first shell are used then the EXAFS-derived CNs provide a more robust determination of the size and shape.[22,27] The plot in Figure 5 gives the dependence of the EXAFS CN on the size of a single close-packed layer of Pt atoms equivalent to a (111) plane of the face-centered cubic (fcc) unit cell. For this layer the Pt–Pt1, Pt–Pt3, and Pt–Pt4 CNs approach 6 for a large sheet (> 30 Å), and there are no Pt–Pt2 neighbors (because they belong in the plane above and below the single sheet of atoms. The CN values and uncertainties (Table 1) define the height of the colored boxes in Figure 5.

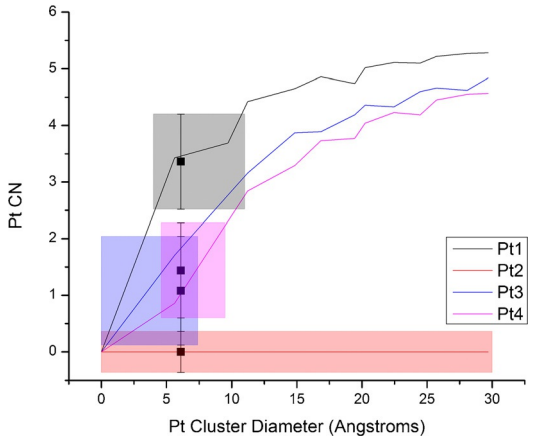

Figure 5. Estimate of Pt cluster diameter from the EXAFS CN assuming that the geometry is a single Pt (111) close-packed plane. The CN values and uncertainties (Table 1) define the height of the colored boxes. The width of the box is determined by the intercept with the curve for defining the dependence of CN on cluster size for Pt-Pt*x* of matching color.

The width of the box is determined by the intercept with the curve for defining the dependence of CN on cluster size for Pt–Pt*x* of matching color, such that the boxes define the size of the sheet that is consistent with each measurement of Pt–Pt*x* CN. At a cluster diameter of 7.25 Å all the boxes overlap along the size axis for the 700 °C reduced sample, indicating that these sized clusters are consistent with the EXAFS measured CNs. At this size value (7.25 Å) the EXAFS CN and associated errors have been plotted to guide the eye. It is important to point out that EXAFS measures the average Pt–Pt*x* CN values and that this interpretation assumes that all the clusters have a similar size and shape. The number of atoms in the clusters can be estimated from the diameter of the cluster, assuming a single layer of Pt atoms. Clusters containing 7 and 13 Pt atoms have diameters of 5.6 and 9.7 Å, respectively. Therefore we estimate that the 7.25 Å diameter clusters contains between 7 and 13 Pt atoms on average.

In addition to the cluster morphology derived from the CN's, the EXAFS-derived interatomic bond lengths also reveal information on potential distortions in the shape of the cluster. Prior work, both experimentally and theoretically, has shown that there can be nonisotropic contraction of the bond length in small Pt clusters.[24,28] For the Pt clusters in the 700 °C reduced sample the Pt cluster interatomic distances for Pt1 and Pt3 are contracted by 2.6 ± 0.2 % compared to the reference bulk values, whereas the Pt–Pt4 distance is contracted by 3.3 ± 0.3 % (see Supporting Information, Figure 3). The additional contraction of the Pt4 distance as compared to the Pt1 and Pt3 distances in the cluster suggest a distortion of the Pt cluster. There are two basic types of distortions that can be envisaged. A distortion in the plane of the cluster is shown in Supporting Information, Figure 4 top. In this case all of the first nearest neighbor distances are affected by the distortion, which is not consistent with the EXAFS results. Another type of distortion, caused by buckling the structure, is shown in Supporting Information, Figure 4 bottom. This type of distortion preserves all the first nearest neighbor distances whereas allowing the Pt–Pt4 distance to contract. In this scenario two of the three Pt–Pt4 distances are contracted whereas the third remains unchanged as shown in Supporting Information, Figure 5. As EXAFS measures the average cluster geometry, it is proposed that this buckling-type of distortion is consistent with the EXAFS data.

Argonne chromatic aberration-corrected (ACAT) TEM

In Figure 6 a–c ACAT TEM images are shown from three different individual Pt clusters acquired from the 0.35 wt % Pt/chlorided γ-alumina sample which was reduced ex situ at 700 °C for

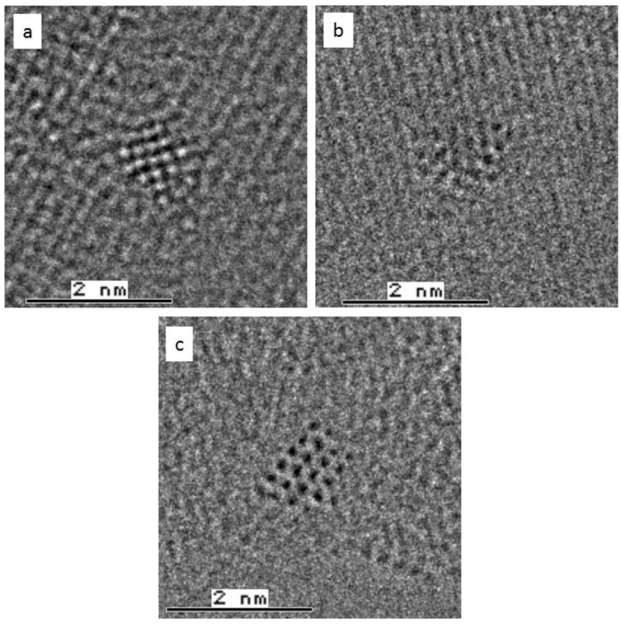

Figure 6. ACAT TEM images of three different individual Pt clusters. Approximate defocus values are a) + 80 Å; b) −20 Å; c) −40 Å.

ten minutes. In each case, the images were acquired as part of a through-focus series with 20 Å steps, and the defocus value was estimated from this step value taking zero defocus to correspond to an image in the center of the series having minimal contrast. For both Figures 6 b,c, the Pt particles are imaged at a defocus within the main Scherzer underfocus interval. The C_s value determined by the alignment procedure was 5.8 μm, which results in a Scherzer defocus interval centered at $-\sqrt{\lambda C_s}$, or approximately −40 Å for a 200 kV illumination. In these images, the Pt atoms are clearly recognizable and appear dark. The image in Figure 6 a is from an overfocus condition, and it is shown again in Figure 7 along with two other images of the series, taken at nominal focus values of 240 Å, 80 Å, and −40 Å. The first two images (Figure 7 a,b) clearly show an ordered, approximately square, array of bright features, with a separation of ≈1.95 Å. This distance is well below the 2.77 Å first neighbor distance in Pt metal, which indicates that the Pt atoms must reside in multiple layers along the beam direction. The distance measured from Figure 7 b is in excellent agreement with the separation of Pt atoms in projec-

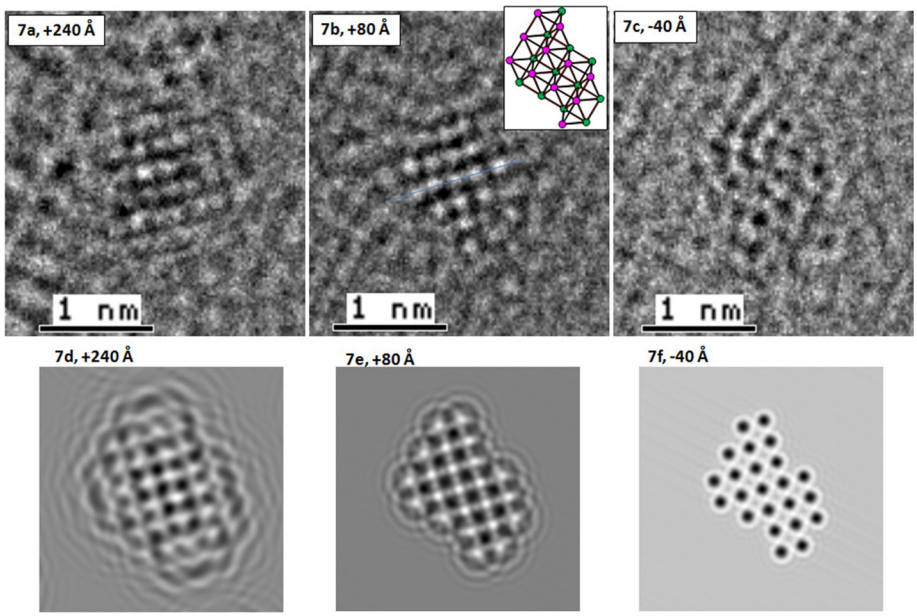

Figure 7. Three images from the same series as Figure 6a. a,b) Square pattern with 1.95 Å repeat; this structure appears to have collapsed by the time 7c was recorded. d–f) Simulated images corresponding to the experimental defocus values for the 23-atom model shown in the inset to 7b.

tion along a [001] zone axis of the fcc cubic cell. The square arrangement of the bright features clearly suggests that the structure of the particle is two or more square layers in a [001] zone axis projection. Based on this, atomic positions were assigned by using the bright features of Figure 7b, and the proposed bilayer model is shown as an inset with each layer color-coded.[29]

Further verification of this was obtained by simulating images according to Equation (1). The calculated images at the defocus values of images Figure 7a–c are shown as corresponding Figure 7d–f. The images were simulated by using two atomic layers of fcc Pt along a [001] zone axis (total thickness is one unit cell, 3.92 Å). The simulated image for 240 Å focus in Figure 7d shows pronounced delocalization, with the occurrence of intensity maxima in the interstitial positions, which is in good agreement with the experimental image in Figure 7a. The image in Figure 7e at 80 Å overfocus shows less delocalization, with intensity maxima at the atomic positions and is also in good agreement with the experimental image in Figure 7b, from which the model was determined.

The final image shown in Figure 7c is in the main Scherzer underfocus interval in which Pt atoms are imaged as dark features. Although dark features indicative of atoms can be seen in the image, the locations of the dark features do not show any ordered pattern, and disagree in their positions with the bright features of Figures 7a,b. The particle had clearly lost its ordered structure when Figure 7c was taken, presumably as a result of atomic displacements induced by the electron beam. Based on an electron dose rate of 300–500 e^{-} Å^{-2} s^{-1} recorded during the session, and a total time exposed to the beam of approximately 20 s (it is the fifteenth image in the series), this suggests that structural deterioration of nanometer-sized Pt particles can readily occur at doses between 0.6×10^{6} and 1.0×10^{6} electrons during TEM imaging at 200 kV.

One property of TEM images, which provides an advantage over high-angle annular dark field (HAADF) AC–STEM, is that features of the catalyst support may be more readily visualized in the images. This is the case for the image shown as Figure 6b, in which planes with approximately 2.0 Å spacing are visible. Based on the allowed spacings in this range for γ-Al_2O_3, this set of planes can be unambiguously identified as (004) planes. In Figure 8, these planes are further emphasized by markings, and the Pt atomic positions are also indicated. As can be seen in Figure 8, the Pt

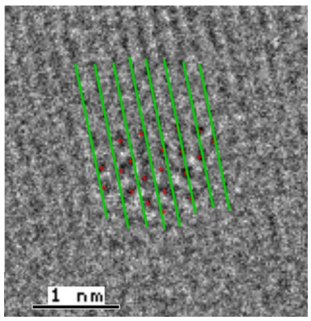

Figure 8. Enlarged version of Figure 7b, with green lines marking the dark-contrast portions of γ-Al_2O_3 (004) planes, and red "+" signs marking the locations of 20 atoms imaged as dark features.

atoms tend to reside preferentially on the dark portion of the (004) contrast oscillation. From this, one can obtain information on the registry of the atoms with the support. The γ-Al_2O_3 structure is a defective spinel,[30] and preferentially forms as plates normal to the [110] direction. The (004) planes oscillate between a high-density segment containing oxygen, octahedral and quasioctahedral aluminum, in between which lie lower density regions containing only tetrahedral Al.[30] Based on the atomic positions determined in Figure 8, the Pt atoms prefer to be situated roughly in registry with the high-density oxygen plus octahedral Al segment of the (004) γ-Al_2O_3 repeat. This location for the Pt atoms is broadly consistent with earlier reports of HAADF STEM on highly dispersed Pt/γ-Al_2O_3, in which the Pt atoms within trimers were also found to occupy sites close to the higher-density portions of the (004) repeat.[2] However, other proposed models of Pt clusters on γ-Al_2O_3 surfaces, such as those from recent DFT calcula-

tions by Mager-Maury et al.,[31] do not correspond to the high density portion of the (0 0 4) planes seen in Figure 8.[31]

The final micrograph in Figure 6c clearly shows another highly ordered structure. As illustrated in Figure 9a, the projected nearest neighbor distances are 2.4 Å and 2.8 Å. As for Figure 6a this again implies that the structure contains atoms at multiple heights. The atomic positions in Figure 6c give an excellent match to the projection of two staggered layers of cubic Pt projected along the [1 1 0] zone axis. In Figure 9a, the match between an unadjusted overlay of the Pt [1 1 0] planes onto the atomic positions is indicated by dark features of the micrograph. A 3-dimensional view of the two staggered planes in the overlay is shown as an inset. To obtain further support for the proposed model, a through-focus image series was simulated using the model shown in Figure 9a inset.

The intensity along the indicated row of six Pt atoms is plotted in Figures 9b,d for the experimental images in the focal series, and the corresponding intensity traces for the simulations are shown in Figures 9c,e. The intensity traces from the image series agree well with most aspects of the simulations including the general form of the variation of intensity at an atomic site as a function of focus, as well as the appearance of artifacts of delocalization in the overfocus regime, specifically some atom-like peaks which are outside of the particle at large overfocus. A feature of the experimental images, which is not reproduced in the simulations, is the decreasing intensity at atomic columns towards the edges of the particle. It is likely that the decreased signal from atoms on or near the particle edges results from less constraint on atomic motion (thermal as well as beam-induced) towards the edges of the ordered Pt cluster, which would cause a broadening and reduction of the electron form factor at those sites. The appearance of more contrast generally in the experimental images in the overfocus regime relative to the simulated contrast is likely owing to the ad-hoc nature of the envelope function $E(U)$ in the current simulations, since the damping imposed by $E(U)$ is the main factor impacting overall contrast levels in the images.

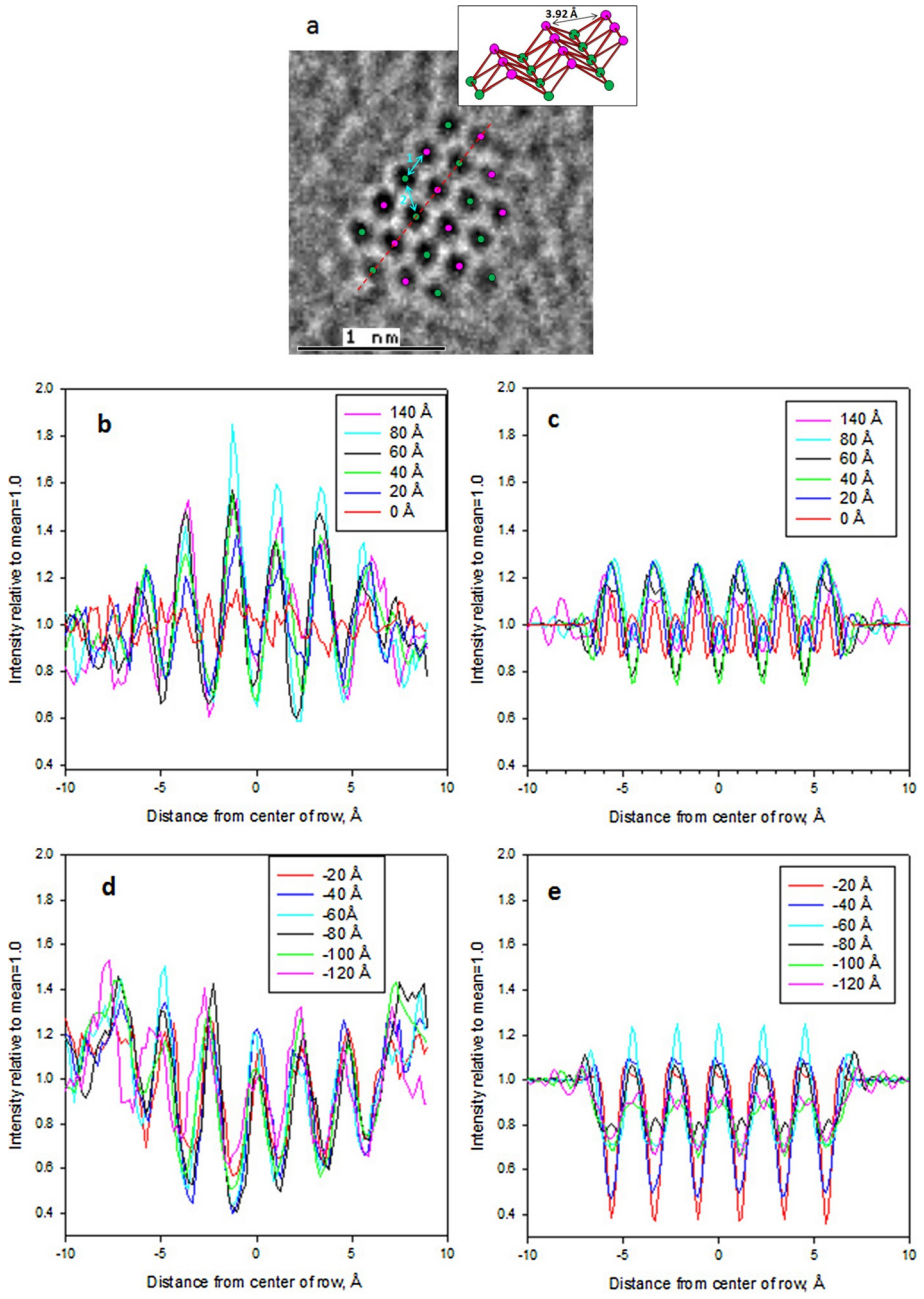

Figure 9. a) Enlarged version of Figure 6c. The distances labeled 1 and 2 in the Figure are 2.4 Å and 2.8 Å respectively. Overlayed on the figure are two (1 1 0) layers of cubic Pt (magenta dots). The 3-dimensional structure model is shown as an inset. Line traces of intensity along the dashed red line in a are shown in d for overfocus and b for underfocus conditions. Corresponding traces from simulated images are shown in c and e.

Discussion

The focus of the present work is a comparison of the information content obtained from AC–STEM, ACAT TEM, and EXAFS with the characterization of the 700 °C hydrogen-reduced 0.35 wt% Pt on chlorided γ-Al_2O_3 as the prototypical catalyst. The AC–STEM data show that after the 700 °C reduction the clusters on the alumina support are present as a narrow particle size distribution centered at

0.88 nm (Figure 1d and Figure 2). The morphology of the Pt particles was studied by using a reported method that involves a redistribution of the atoms using a high electron dosage.[15] The data show that the particles are present in an oblate (disk-like) morphology with a thickness of one to two atomic layers (Figure 3, Supporting Information, Figure 2). Both of these methods involve the study of only a very small amount of sample and there is always a question of whether the results are representative of the sample at-large. To address this, in situ XAFS data at the Pt L_3-edge were collected to obtain structural information representative of the average of all of the Pt in the sample. These data (Figures 4 and 5, and Table 1) are consistent with the STEM data; on average the Pt clusters are present as flattened clusters with an average diameter of 0.72 nm with some distortion to the cluster geometry, which is consistent with a buckling of the oblate cluster. Thus, the Pt remains well-dispersed on the γ-Al_2O_3 even after reduction at 700 °C implying that there is clearly a strong interaction between the cluster and the support. It is acknowledged that there is a slight difference in the sample handling between the STEM and XAFS, with slight air exposure during the preparation of the electron microscopy samples whereas the XAFS data were obtained in situ in the presence of adsorbed hydrogen. However, the agreement in the particle size (0.72 vs. 0.88 nm, which is within the error bar of the EXAFS measurement) and the particle shape implies that the brief air exposure at room temperature after reduction has little effect on the Pt cluster morphology. Our results of the observation of two-dimensional morphology of supported Pt clusters after high temperature reduction are in agreement with prior work, in which the Pt was reduced at 450 °C.[6]

Other trends found by XAS for high-temperature heat treatment are a decrease in the bond length for the first-neighbor Pt–Pt1 coordination shell, with a distance of 2.72 ± 0.01 Å at 450 °C from the bulk value of 2.77 Å, and a steadily increasing number of Pt bonds to support oxygen with increasing temperature[6,14] which suggests a stronger interaction with the alumina support, which could be related to the continued dehydroxylation of the alumina as the temperature is increased.[6]

The XAS and STEM cluster size and atom-counting information lead to a consistent picture of how clusters evolve a more two-dimensional and more strained structure, with closer support interactions at high temperature, whereas the ACAT TEM images provide a basis for direct structure determination of individual clusters. STEM imaging has been used previously to determine the structure of supported metal nanoclusters supported on MgO,[32] however it is likely that the MgO support would result in stronger interaction with the metal atoms, which may reduce their tendency to displace under a focused sub-Ångstrom electron probe. For the current Pt supported on γ-Al_2O_3, the ACAT TEM imaging appears to provide an advantage for structure determination relative to AC–STEM because of the reduced tendency for the structures to deteriorate under the electron beam. This use of aberration-corrected TEM, which uses a broad coherent electron beam, can thus offer advantages relative to STEM for structure determination of fine clusters. The use of TEM in the current work was confined to consideration of particles in the range of 1.0–1.2 nm, and in spite of some apparent benefits relative to beam damage it is doubtful that TEM imaging will be able to image much finer clusters having, for example, five or fewer atoms. The unambiguous imaging of such fine clusters is, for the present, an area in which probe-corrected HAADF–STEM remains unchallenged.

To address the structural evolution of Pt clusters with changing reduction temperature, a number of hurdles still need to be addressed. It will be necessary to determine structures on a statistically significant number of clusters for a range of reduction temperatures, and it is clear from the current work on three distinct clusters at a single reduction temperature that a central challenge will be to obtain optimum efficiency in data collection and processing. In addition to the need for vastly increasing the number of clusters analyzed, a number of potential artifacts need to be carefully considered. An important potential artifact is the possibility that changes to structures may occur owing to air exposure during sample preparation. The current choice of sample preparation using an ethanol suspension was dictated by problems with sample stability for a preparation without solvent, such as was used for the STEM examination. Further development of this technique needs to carefully consider potential changes caused by a range of sample preparations, preferably supported by data from techniques such as XAS for which artifacts of sample handling and preparation can be kept to a minimum.

The three Pt clusters presented in Figure 6a–c all have quite distinct structures, which supports a polydisperse nature for the structures of individual Pt clusters supported on γ-Al_2O_3 even though the cluster size distribution is quite narrow (Figure 2). Figures 6a,c both clearly have ordered structures consistent with fcc Pt, though their structures differ from each other since the planes in contact with the support are (1 0 0) and (1 1 0) types respectively. The current work has applied image simulation to model the intensities seen in the corresponding through-focus series. The use of simulation and modeling of intensities is critical for TEM structural studies, to provide information on the thickness of the clusters or the number of superimposed atoms. The current modeling provides adequate agreement with structures containing two staggered atomic layers (with no direct superposition of atoms), however, more work is needed to improve the quantitative match and narrow the margin of error on the structures themselves. In spite of the preliminary stage of the modeling, it should be noted that the structures proposed here for Figures 6a,c are consistent with the result from the STEM atom counting that the cluster thicknesses tend to be intermediate between a monolayer and a bilayer, and from the EXAFS modeling which is consistent with such a planar-like structure. Specifically, the projected density of two staggered (1 0 0) planes is in the correct range, equivalent to 1.73 times the areal density of a single close-packed (1 1 1) plane, whereas the projected density of two staggered (1 1 0) planes is 1.22 times that of the close-packed monolayer. We have also employed a model corresponding to Figures 9c,e in which a single ad-atom was superimposed on top of one of the atoms in a third plane. This

led to a large increase in the intensity deficit in that column for simulated images in the Scherzer underfocus interval, so that its deficit was approximately double that of adjacent columns. This further supports our conclusion of a plate-like morphology with small and uniform thickness for these two ordered particles.

As mentioned above, the decrease of Pt–Pt1 first-neighbor distance at treatment temperatures above about 350 °C is a feature of the Pt EXAFS which suggests increased bonding with the support and resulting strain within the clusters. In light of this expectation, the ordered structures of the clusters shown in Figures 6a,c is perhaps surprising. It is hard to rule out the possibility that these ordered structures might have been modified by air and solvent exposure during sample preparation and transport to the ACAT. This could for example result in rehydroxylation of the support/cluster interface and relaxation of the structure to the observed ordered configurations. Another possible explanation for the observation of ordered clusters in Figure 6a and 6c is that they are slightly larger at 1.0–1.2 nm than the 0.7–0.9 nm average sizes indicated from STEM and EXAFS, and that the degree of order is size dependent.[25] In contrast to these two particles, the particle shown in Figure 6b has a much less ordered structure, suggestive of significant strain. As already discussed, the Pt atomic positions may correlate with specific sites within (004) planes of the γ-Al_2O_3 spinel structure, which might plausibly result in strains within the cluster. An important goal for future work in this area is to determine the preponderance of the more ordered type of cluster (Figures 6a,c) relative to more highly strained particles whose atoms occur in a fixed registry with support features.

Experimental Section

A single catalyst formulation was studied in the current investigation, consisting of a 0.35 wt% Pt on chlorided γ-Al_2O_3 with 160 $m^2 g^{-1}$ BET surface area by nitrogen adsorption. The Pt concentration was determined by using inductively coupled plasma atomic absorption spectroscopy. Starting from a fully oxidized initial state, the catalyst was subjected to reduction treatments in a flow of 100% H_2 at a range of temperatures using a ramp rate of 10 °C $minute^{-1}$. The sample was then held at the reduction temperature for 10 min, followed by cooling to room temperature in the same 100% H_2 atmosphere.

STEM examinations were performed on samples in the reduction series. Samples were prepared by dry grinding with an agate mortar and pestle in ambient air, then contacting a supported lacy carbon film to the ground sample fines. The STEM results were obtained using an FEI-Titan 80–300 STEM operated at 200 kV accelerating voltage in HAADF imaging mode, with a probe current of approximately 60 pA. The instrument had a point resolution of 0.8 Å and was equipped with a high-sensitivity array of four large-angle silicon drift detectors for ultra-high sensitivity local chemical analysis (ChemiStem). Particle sizes were measured using Image-Pro software. An average feret diameter was calculated for each individual particle by taking the diameter for every orientation of the particle in the image. Morphological evaluation of the particles was achieved using a method involving a redistribution of the atoms using a high electron dosage, described in Sanchez et al.[15]

TEM imaging was performed on the 700 °C reduced sample, which was prepared by dry grinding and dispersing in dry ethanol followed by placing a droplet of the suspension on a supported lacy-carbon grid. The TEM imaging of this sample was performed by using the Argonne Chromatic Aberration-corrected TEM (ACAT) instrument, with an image corrector to correct both spherical and chromatic aberration. ACAT has resolution better than 0.8 Å when operated at 200 kV. Using the ACAT, through-focus image series were acquired from individual supported Pt clusters, using a defocus step of 20 Å between images.

The XAFS spectra were collected in fluorescence yield mode at the MR-CAT beamline 10ID at the Advanced Photon Source at Argonne National Laboratory.[16] The insertion device X-ray beam was defined to be approximately 1 mm in both the vertical and horizontal. A double crystal monochromator with Si(111) crystals was used to select the incident X-ray energy. X-rays of higher harmonic energies were minimized using a Rh-coated mirror. The X-ray energy was calibrated by using a Pt foil, which was also collected with the measured data by using a reference ionization chamber. The ionization chamber gases were optimized for the transmitted and reference X-ray intensity measurements. The fluorescence signal was recorded using a Stern–Heald detector filled with Kr gas. The Pt L_3-edge XAFS data from the Pt/γ-Al_2O_3 catalyst were collected in situ using a custom designed XAFS cell.[17] The previously 700 °C reduced sample was re-reduced in situ by ramping to 700 °C at 10 ° min^{-1} in a flow of 100% hydrogen, followed by a short dwell at 700 °C. The sample was cooled to RT in the hydrogen and XAFS data were collected at RT.

Image Simulations

Simulations of ACAT TEM images were performed by using a linear imaging approximation, with image contrast approximated according to Equation (1):[18]

$$I(U) = \delta(0) + E(U) \times [\Psi_0(U) \exp\{-i\chi(U)\} + \Psi_0^*(-U) \exp\{i\chi(-U)\}] \quad (1)$$

Where U is the position vector in the instrument back focal plane (|U| is the spatial frequency), E(U) is a coherence envelope modeled on a focal spread of 5 Å,[19] $\Psi_0(U)$ is the Fourier transform of the scattered part of the exit wave and $\chi(U)$ is the phase shift induced by the defocus and other lens aberrations.[18,19] The exit wave $\Psi_0(U)$ was calculated using multislice to a resolution of 3 $Å^{-1}$. The support was not included in the calculations, which is justifiable as long as there are no strongly excited Bragg reflections, and the support image contrast is thus much smaller than that of the superimposed Pt clusters. With the exception of defocus and astigmatism, the aberration coefficients used in χ(U) were those determined by the ACAT alignment software at the time the images were recorded, including a C_s value of 5.8 μm. (Owing to the particles that are thin and only ≈1 nm in size, the amplitude part of the wave is weaker than the phase, so C_s was tuned to a larger value. The reason for using a positive C_s value instead of negative C_s value is to compensate the negative C5 value for the ACAT instrument). For the small thicknesses considered in this work, the calculated images using Ψ_0(U) from multislice calculations does not differ noticeably from a phase object approximation, while the use of a weak phase object approximation shows only small discrepancies from the multislice or phase object result.

EXAFS Modeling

Data processing and fitting were conducted using the programs Athena and Artemis[20] and FEFF6.0[21] for the theoretical calculations based on structure of bulk fcc Pt. The EXAFS models include single and multiple scattering paths[22,23] from Pt and also a long Pt-support O signal.[6] Each of the 4 shells of Pt atoms about the absorbing (Pt0) atom is denoted with the nomenclature of Pt1, Pt2, Pt3, and Pt4. These paths and their parameterization are listed in the Supporting Information, Table 1. There are 12 parameters used to describe the model: 5 coordination numbers (CN), 3 parameters to describe changes in path length (ΔR), 2 Debye temperatures (T_d), one σ^2-value, and an energy shift parameter (ΔE). The ΔR values for the paths associated with the Pt cluster are described in terms of an expansion/contraction term α which is a constant factor multiplied by the reference path length (Reff). The 4th shell required an independent α value. The mean square displacement values (σ^2) are described in terms of a Debye model with characteristic Debye temperature T_d. The value for S_0^2 (0.93 ± 0.05) was determined from Pt foil. The data range from 3.5 to 10 Å^{-1} was used in the Fourier transform with *k*-weight of 1, 2 and 3. The initial model was applied to the Fourier-transformed range of 1.5 to 6.0 Å, containing 18 independent points and 12 parameters. Further tests were performed to determine if each of the Pt shells required independent α and T_d values. Comparisons of the reduced-χ^2 values were made over the data range dominated by the higher shells from 3.2 to 6.0 Å containing 14 independent points and 6 parameters. This modeling approach is similar to that used previously for Pt nanoparticles.[24]

Table 1. Pt EXAFS modeling results for the 0.35 wt% Pt/γ-Al_2O_3 sample reduced in situ at 700 °C in H_2. Path is the scattering path; CN is the coordination number; *R* is the interatomic distance; σ^2 is the mean square displacement of *R*. Only values for single scattering paths are reported.[17][a]

Path	CN	*R* [Å]	σ^2 [$\times 10^{-3}$ Å^2]
Pt0–O	1.9 ± 0.3	2.50 ± 0.01	1.6 ± 1.2
Pt0–Pt1	3.3 ± 0.7	2.70 ± 0.01	4.4 ± 1.1
Pt0–Pt2	0.0 ± 0.3	3.81 ± 0.01	5.4 ± 1.1
Pt0–Pt3	1.6 ± 0.8	4.67 ± 0.01	5.5 ± 1.1
Pt0–Pt4	1.9 ± 0.8	5.35 ± 0.01	8.5 ± 2.3

[a] See Supporting Information, Table 2, for a list of all EXAFS parameters.

Acknowledgements

AC–TEM imaging was accomplished at the Electron Microscopy Center—Center for Nanoscale Materials at Argonne National Laboratory, a U.S. Department of Energy Office of Science Laboratory operated under Contract No. DE-AC02-06CH11357 by UChicago Argonne, LLC. Use of the Advanced Photon Source, an Office of Science User Facility operated for the U.S. Department of Energy (DOE) Office of Science by Argonne National Laboratory, was supported by the U.S. DOE under Contract No. DE-AC02-06CH11357. MRCAT operations are supported by the Department of Energy and the MRCAT member institutions.

Keywords: electron microscopy · nanostructures · platinum · supported catalysts · X-ray absorption spectroscopy

[1] "UOP Platforming Process": N. Dachos, A. Kelly, D. Felch, E. Reis, in *Handbook of Petroleum Refining Processes* (Ed.: R. A. Meyers), McGraw-Hill, New York, **1996**, pp. 3–26.
[2] P. D. Nellist, S. J. Pennycook, *Science* **1996**, *274*, 413–415.
[3] L. Y. Chang, A. S. Barnard, L. C. Gontard, R. E. Dunin-Borkowski, *Nano Lett.* **2010**, *10*, 3073–3076.
[4] M. K. Oudenhuijzen, P. J. Kooyman, B. Tappel, J. A. van Bokhoven, D. C. Koningsberger, *J. Catal.* **2002**, *205*, 135–146.
[5] A. Munoz-Paez, D. C. Koningsberger, *J. Phys. Chem.* **1995**, *99*, 4193–4204.
[6] M. Vaarkamp, J. T. Miller, F. S. Modica, D. C. Koningsberger, *J. Catal.* **1996**, *163*, 294–305.
[7] F. Behafarid, L. K. Ono, S. Mostafa, J. R. Croy, G. Shafai, S. Hong, T. S. Rahman, S. R. Bare, B. R. Cuenya, *Phys. Chem. Chem. Phys.* **2012**, *14*, 11766–11779.
[8] A. L. Ankudinov, J. J. Rehr, J. J. Low, S. R. Bare, *Top. Catal.* **2002**, *18*, 3–7.
[9] H. Mistry, F. Behafarid, S. R. Bare, B. R. Cuenya, *ChemCatChem* **2014**, *6*, 348–352.
[10] J. H. Kang, L. D. Menard, R. G. Nuzzo, A. I. Frenkel, *J. Am. Chem. Soc.* **2006**, *128*, 12068–12069.
[11] S. I. Sanchez, L. D. Menard, A. Bram, J. H. Kang, M. W. Small, R. G. Nuzzo, A. I. Frenkel, *J. Am. Chem. Soc.* **2009**, *131*, 7040–7054.
[12] A. L. Ankudinov, J. J. Rehr, S. R. Bare, *Phys. Rev. Lett.* **2001**, *86*, 1642–1645.
[13] J. E. Mondloch, E. Bayram, R. G. Finke, *J. Mol. Catal. A* **2012**, *355*, 1–38.
[14] W. Sinkler, S. R. Bare, S. D. Kelly, *Microsc. Microanal.* **2013**, *19*, 1682–1683.
[15] S. I. Sanchez, S. A. Bradley, W. Sinkler, *Microsc. Microanal.* **2012**, *18*, 1036–1037.
[16] C. U. Segre, et al., The MRCAT Insertion Device Beamline at the Advanced Photon Source. in Synchrotron Radiation Instrumentation: Eleventh U. S. National Conference. **1999**. Stanford, CA: American Insitute of Physics.
[17] S. R. Bare, G. E. Mickelson, F. S. Modica, A. Z. Ringwelski, N. Yang, *Rev. Sci. Instrum.* **2006**, *77*, 023105.
[18] W. O. Saxton, *J. Microsc.* **1995**, *179*, 201–213.
[19] M. Haider, H. Müller, S. Uhlemann, J. Zach, U. Loebau, R. Hoeschen, *Ultramicroscopy* **2008**, *108*, 167–178.
[20] B. Ravel, M. Newville, *J. Synchrotron Radiat.* **2005**, *12*, 537–541.
[21] S. I. Zabinsky, J. J. Rehr, A. Ankudinov, R. C. Albers, M. J. Eller, *Phys. Rev. B* **1995**, *52*, 2995.
[22] A. I. Frenkel, *J. Synchrotron Radiat.* **1999**, *6*, 293–295.
[23] A. Witkowska, A. Di Cicco, E. Principi, *Phys. Rev. B* **2007**, *76*, 104110.
[24] S. D. Kelly, M. E. Charochak, S. R. Bare, *J. Phys. Conf. Ser.* **2013**, *430*, 012061.
[25] S. A. Bradley, W. Sinkler, D. A. Blom, W. Bigelow, P. M. Voyles, L. F. Allard, *Catal. Lett.* **2012**, *142*, 176–182.
[26] A. Mayoral, D. A. Blom, M. M. Mariscal, C. Guiterrez-Wing, J. Aspiazu, M. Jose-Yacaman, *Chem. Commun.* **2010**, *46*, 8758–8760.
[27] A. I. Frenkel, C. W. Hills, R. G. Nuzzo, *J. Phys. Chem. B* **2001**, *105*, 12689–12703.
[28] A. L. Ankudinov, J. J. Rehr, J. J. Low, S. R. Bare, *J. Chem. Phys.* **2002**, *116*, 1911–1919.
[29] L. D. Marks, D. J. Smith, *Nat. Chem.* **1983**, *303*, 316–317.
[30] R.-S. Zhou, R. L. Snyder, *Acta Crystallogr. Sect. B* **1991**, *47*, 617–630.
[31] C. Mager-Maury, C. Chizallet, P. Sautet, P. Raybaud, *ACS Catal.* **2012**, *2*, 1346–1357.
[32] V. Ortalan, A. Uzun, B. C. Gates, N. D. Browning, *Nat. Nanotechnol.* **2010**, *5*, 843–847.

Received: July 15, 2015
Published online on October 23, 2015